ILASS 2008
Sep. 8-10, 2008, Como Lake, Italy

Paper ID ILASS08-2-19

ASSESSMENT OF GAS AND LIQUID FLUXES INDUCED BY LIQUID DROP FALLING ONTO A SMOOTH DRY PLATE

B. H. Bang[1], S. S. Yoon[1*], H. Y. Kim[1], R. A. Jepsen[2], S. D. Heister[3], H. Park[4], S. C. James[5]

[1]Department of Mechanical, Korea University, Anamdong, 5-Ga, Sungbukgu, 136-713, Seoul, Korea.
[2]Mechanical Environments, Sandia National Labs, P.O. Box 5800, Albuquerque, NM 87185, USA.
[3]School of Aeronautics and Astronautics, Purdue Univeristy, West Lafayette, IN, 47907, USA.
[4]ADD, 3-Hyun-3, 111 Sunam-Dong, Yuseong-Gu, Taejon 305-152, Korea.
[5]Thermal/Fluid Science & Engineering, Sandia National Labs, P.O. Box 969, Livermore, CA 94551, USA.

ABSTRACT

The two-phase flow model using the boundary element method was applied to investigate the physics of a falling liquid drop impacting onto a solid, dry plate. Xu et al. (*Physical Review Letter*, 2005) showed that the air pressure plays an important role in splashing: when the air pressure was substantially reduced (i.e., from 100 to 17 kPa), splashing of an ethanol drop with Weber number close 838 was suppressed. This remarkable discovery by Xu et al. is the motivation behind our current modeling effort. We investigate the air pressure effect on the appearance of splashing under the presumption that the Kelvin-Helmholtz instability plays a critical role in causing the splashing. Gas fluxes near the compressed region induced below the falling drop were computed at random locations. The computation showed that the gas flux was relatively high, especially compared to the drop impact speed. High gas flux is caused by acceleration of gas out of the compressed region. We believe that vorticity generated by the escaping gas may be a sufficient disturbance to rupture the drop's bottom surface. Our preliminary computations show that the surrounding air velocity exceeds 3 times the drop's impact speed. This shear-driven instability may eventually lead to splashing, which has been previously characterized in the famous *milk-drop crown*experiments.

Keywords: *BEM, Two-phase flow, Drop impact, Kelvin-Helmholtz instability, Splashing*

INTRODUCTION

Drop impact phenomena are readily encountered in raindrop impact and in numerous industrial applications such as inkjet printing, painting, spray-wall impact within IC-engines, and fire suppression sprays. As shown in classical experiments [1-2], a drop will stick to the impacting substrate when the drop surface tension energy is not high enough to overcome the drop's dissipative energy [3]. Upon sticking, the drop spreads radially and forms a toroidal ring when it has a relatively low Weber number. At intermediate Weber numbers, an azimuthal instability develops and forms "fingers" at the rim of the spreading ring. If the Weber number is increased, the drop "splashes" upon contact with the substrate and the fingers shed additional individual drops. In this paper, we are particularly interested in the splashing mechanism and its relevant modeling, and use the boundary element method (BEM).

The BEM is suitable for drop impact modeling because it accurately tracks the changing morphology of the impacting drop while the Volume-of-Fluid (VOF) approach tends to smear out the interface between the liquid and gas.

The pioneering BEM work for the drop impact study was conducted by Yarin and Weiss [4] with subsequent relevent work by Weiss and Yarin [5], Davidson [6, 7], and Park et al. [8]. In most modeling efforts, a drop is initially assumed to be in contact with the impacting substrate or liquid-film and, therefore, the compressed air effect due to a falling drop is neglected. Because air effects are not simulated in these models, the fundamental mechanism of splashing cannot be properly addressed despite confirmation confrimed that compressed air is instrumental in causing the splashing; see Xu et al's experiment [9, 10].

Park et al. [8] attempted to address air effects on drop impact, but they noted that their axisymmetric model was not capable of simulating the actual splashing of a 3D event. In this paper, we attempt to circumvent Park et al.'s dilemma by introducing a quasi-3D model; that is, applying the vortex-ring instability analysis to the snap-off ring or rising corona to predict the number of splashed droplets. The vortex-ring

*Corresponding author: skyoon@korea.ac.kr

analysis used herein is based on the linear theory of Ponstein and, thus, we caution that neither the nonlinear formation of the satellite droplets nor capillary merging (which tends to reduce the number of splashed droplets) can be addressed using the current quasi-3D model.

Our quasi-3D splashing model is unique in that it considers the compressed air effect on drop impact while modeling splashing of the 3D event. In this paper, we qualitatively show that the newly implemented quasi-3D model produces seemingly plausible results though further quantification of the computataional results in comparison with experimental data is needed.

Our preliminary computation includes the accelerated gas fluxes near the compressed region and their effects on liquid. Random numbers are uniformly seeded inside the computational domain where local velocities (or fluxes) of liquid and gas phases are calculated.

MODELING DESCRIPTION

Two Phase Flow Modeling

Heister [11] provides a complete description of the basic modeling elements involved in a BEM application to two-phase flows. In an inviscid, incompressible, axisymmetric flow, it is presumed that the flow dynamics are governed by Laplace's equation: $\nabla^2\phi = 0$. The BEM uses an integral representation of this equation to provide a connection between the values on the boundary, the local geometry, and the local velocity normal to the boundary, $q = \partial\phi/\partial n$, as follows:

$$\alpha\phi(\vec{r}_i) + \int_\Gamma \left[\phi \frac{\partial G}{\partial \hat{n}} - qG \right] \mathrm{d}\Gamma = 0, \tag{1}$$

where $\phi(\vec{r}_i)$ is the value of the potential at a point $\vec{r}_i$, S is the boundary of the domain, α is the singular contribution when the integral path passes over the "base point," and G is the free-space Green's function corresponding to Laplace's equation. For an axisymmetric domain, the free-space Green's function can be expressed in terms of elliptic integrals of the first and second kinds and is a function solely of the instantaneous surface geometry. For this reason, a discrete representation of Eq. (1) can be cast as a linear system of equations relating local ϕ and q values. In the discretization, both ϕ and q are assumed to vary linearly along each element thereby providing a formal second-order accuracy for the method. Because the resulting integrals do not have exact solutions in this case, four-point Gaussian quadrature is used to maintain a high accuracy of integration and to preserve the second-order accuracy overall.

While this governing equation is linear, nonlinearity in these free-surface problems enters through the boundary condition at the interface. The unsteady Bernoulli equation provides a connection between the local velocity potential and the surface shape at any instant in time. Prior formulations [11-12] have provided a derivation of this result that is suitable for implementation into a Lagrangian surface tracking environment. The dimensionless form of the unsteady Bernoulli equation for a liquid surface is given below. The three characteristic parameters in these equations are drop radius (a), the impact speed (U), and the liquid density (ρ_l).

$$\frac{\partial\varphi}{\partial t} + \frac{1}{2}\left|\nabla\varphi\right|^2 + P_{gas} + \frac{\kappa}{We} - \frac{Bo}{We} z = 0, \tag{2}$$

where κ is the local surface curvature. The Weber and Bond numbers are defined as $We = \rho_l U^2 a/\sigma$ and $Bo = \rho_l g a^2/\sigma$, respectively, where σ is the fluid surface tension. The Eulerian-Lagrangian transformation for surface nodes moving with the velocity of the liquid is:

$$\frac{D()}{Dt} = \frac{\partial()}{\partial t} + \nabla\phi\cdot\nabla(), \tag{3}$$

where *D/Dt* denotes a material or Lagrangian derivative. Using this transformation, the dimensionless Bernoulli equation at the free surface of the liquid becomes:

$$\frac{D\varphi}{Dt} = \frac{1}{2}\left|\nabla\varphi\right|^2 - P_g - \frac{\kappa}{We} + \frac{Bo}{We} z. \tag{4}$$

Physically, this Bernoulli equation is in a Lagrangian form that is suitable for fluid elements moving with the local velocity of the free surface. Equation (4) includes the effects from dynamic pressure, local gas-phase pressure, capillary pressure, and hydrostatic pressure, respectively.

An analogous treatment for the gas phase yields:

$$\varepsilon\frac{D\varphi_g}{Dt} = \varepsilon\nabla\varphi\cdot\nabla\varphi_g - \frac{\varepsilon}{2}\left|\nabla\varphi_g\right|^2 - P_{gas}, \tag{5}$$

where ε is the gas/liquid density ratio ($\varepsilon = \rho_g/\rho_l$). Mathematically, Eqsuations (4) and (5) provide a system of relations to describe the evolution of the free surface. These nonlinear boundary conditions are coupled at the interface between the gas and liquid phases. Because the gas nodes on the interface are set to be coincident with the nodes in the liquid phase, the liquid velocity is used to advect both sets of nodes on the interface. The kinematic boundary condition provides the necessary relationships to integrate this motion:

$$\begin{aligned} \frac{Dz}{Dt} &= u = \frac{\partial\varphi}{\partial s}\cos\beta - q\sin\beta, \\ \frac{Dr}{Dt} &= v = \frac{\partial\varphi}{\partial s}\sin\beta + q\cos\beta, \end{aligned} \tag{6}$$

where β is the local slope of the wave with respect to the horizontal direction and r and z are the radial and axial coordinates, respectively. Equations (4) through (6) are integrated in time using a 4th-order Runge-Kutta scheme to provide the evolution of the velocity potential and the motion of the free surface. For long integrations or resolution of highly distorted surfaces, points on the free surface will tend to bunch in regions of higher curvature as a result of the free-surface motion. For this reason, the points on the free surface are redistributed at each time step using a cubic spline fitting of the instantaneous shape. Fourth-order accuracy is also employed in computing all surface derivatives to maximize the accuracy of the surface evolution method. The Laplace equation is solved to update velocities and the process continues for a set period.

Interior Flux Computation

To compute the gas fluxes, $\partial\phi_i/\partial z$ and $\partial\phi_i/\partial r$, at any random point within the computational domain, one may take derivatives of the velocity potential of the Laplace equation of (1). Equation (1) with α set to 2π still holds for interior nodes. However, when solving for ϕ at an interior node, the integral over the boundary does not include any nodes on the interior. Because of this, the singularities that arise in the elliptic integral for boundary nodes when the segment contains a base point on the boundary do not occur because the segment will never contain the base point. To calculate ϕ at an interior node, Equation (1) can be rearranged:

$$\phi_i = \frac{1}{4\pi}\int_\Gamma \left[\phi \frac{\partial G}{\partial n} - qG \right] d\Gamma. \quad (7)$$

Following the same discretization procedure used for nodes on the boundary, Equation (1) becomes:

$$2\pi\phi_i = D_{i,j}\phi_j - S_{i,j}q_j \quad (8)$$

where subscript i denotes interior nodes on and subscript j denotes nodes on the boundary. When solving for an individual interior node, D and S become row vectors and thus the value of ϕ_i is given by this single equation. D and S must already be known before ϕ_i can be calculated from Equation (8). Therefore, Laplace's equation must be solved for nodes on the boundary before nodes in the interior.

The free space Green's function solution to the axisymmetric Laplacian is:

$$G = \frac{4rK(p)}{\sqrt{a}}, \quad (9)$$

and from Heister [11],

$$\frac{\partial G}{\partial n} = \frac{-2}{\sqrt{a}}\left\{ n_r K(p) + \frac{E(p)}{c}\left[dn_r + 2rn_z(z-z_i)\right]\right\}, \quad (10)$$

where p, a, c, and d are defined as:

$$p = \frac{(r-r_i)^2 + (z-z_i)^2}{(r+r_i)^2 + (z-z_i)^2}, \quad (11)$$

$$a = (r+r_i)^2 + (z-z_i)^2, \quad (12)$$

$$c = (r-r_i)^2 + (z-z_i)^2, \quad (13)$$

$$d = r^2 - r_i^2 - (z-z_i)^2. \quad (14)$$

And so, differentiating Equation (7) with respect to the base points, it is seen that,

$$\frac{\partial \phi_i}{\partial z} = \frac{1}{4\pi}\int_\Gamma \left[q\frac{\partial G}{\partial z_i} - \phi \frac{\partial^2 G}{\partial n \partial z_i}\right] d\Gamma, \quad (15)$$

$$\frac{\partial \phi_i}{\partial r} = \frac{1}{4\pi}\int_\Gamma \left[q\frac{\partial G}{\partial r_i} - \phi \frac{\partial^2 G}{\partial n \partial r_i}\right] d\Gamma, \quad (16)$$

where,

$$\frac{\partial^2 G}{\partial n \partial z_i} = \frac{-2(z-z_i)}{a^{3/2}}A - \frac{2}{\sqrt{a}}(B+C+H), \quad (17)$$

$$\frac{\partial G}{\partial z_i} = \frac{16r^2 r_i (z-z_i)}{\sqrt{a^5}}F_1(p) + \frac{4r(z-z_i)K(p)}{\sqrt{a^3}}, \quad (18)$$

$$\frac{\partial^2 G}{\partial n \partial r_i} = \frac{2(r+r_i)}{\sqrt{a^3}}L - \frac{2}{\sqrt{a}}(M + NO + P), \quad (19)$$

$$\frac{\partial G}{\partial r_i} = \frac{-8r\left[rr_i^2 - r^3 - r(z-z_i)^2\right]}{\sqrt{a^5}}F_1(p) - \frac{4(r+r_i)rK(p)}{\sqrt{a^3}}, \quad (20)$$

and,

$$A = K(p)n_r + \frac{E(p)}{c}\left[dn_r + 2r(z-z_i)n_z\right], \quad (21)$$

$$B = \frac{4n_r(z-z_i)rr_i}{a^2}F_1(p), \quad (22)$$

$$C = \left[\frac{-4(z-z_i)rr_i}{ca^2}F_2(p) + \frac{2(z-z_i)E(p)}{c^2}\right]\left[dn_r + 2r(z-z_i)n_z\right], \quad (23)$$

$$H = \frac{E(p)}{c}\left[2(z-z_i)n_r - 2rn_z\right], \quad (24)$$

$$L = K(p)n_r + \frac{E(p)}{c}\left[dn_r + 2r(z-z_i)n_z\right], \quad (25)$$

$$M = \frac{-2n_r\left[rr_i^2 - r^3 - r(z-z_i)^2\right]}{a^2}F_1(p), \quad (26)$$

$$N = \frac{2\left[rr_i^2 - r^3 - r(z-z_i)^2\right]}{ca^2}F_2(p) + \frac{2(r-r_i)E(p)}{c^2}, \quad (27)$$

$$O = dn_r + 2r(z-z_i)n_z, \quad (28)$$

$$P = \frac{2E(p)n_r r_i}{c}. \quad (29)$$

$F_1(p)$ and $\underline{F_2}(p)$ are integrals that result from differentiation of the elliptic integrals in the original Equation (7). They are defined as,

$$F_1(p) = \int_0^{2\pi} \frac{\sin^2\Psi}{\sqrt{\left[1-(1-p)\sin^2\Psi\right]^3}} d\Psi, \quad (30)$$

$$F_2(p) = \int_0^{2\pi} \frac{\sin^2\Psi}{\sqrt{1-(1-p)\sin^2\Psi}} d\Psi, \quad (31)$$

and are related to the elliptic integrals $K(p)$ and $E(p)$ as follows:

$$F_1(p) = \frac{-a^2}{4(z-z_i)rr_i}\frac{\partial E}{\partial z_i} = \frac{a^2}{2\left[rr_i^2 - r^3 - r(z-z_i)^2\right]}\frac{\partial E}{\partial r_i}, \quad (32)$$

$$F_2(p) = \frac{a^2}{4(z-z_i)rr_i}\frac{\partial K}{\partial z_i} = \frac{-a^2}{2\left[rr_i^2 - r^3 - r(z-z_i)^2\right]}\frac{\partial K}{\partial r_i}, \quad (33)$$

The integrals $F_1(p)$ and $\underline{F_2}(p)$ are calculated numerically using Simpson's One-Third Rule.

It is important to note that the $\partial\phi/\partial z_i$, $\partial q/\partial z_i$, $\partial\phi/\partial r_i$, and $\partial q/\partial r_i$ terms obtained when differentiating Equation (7) are all equal to zero because the boundary q and ϕ values do not depend on the interior point; i.e., $\partial\phi/\partial z_i = \partial\phi/\partial r_i = 0$ $\partial q/\partial z_i = \partial q/\partial r_i = 0$. The derivatives were taken with respect to the base points. The q and ϕ terms that are integrated in Equation (7) are values at the field points (on the boundary of the domain) and are not a function of the z_i and r_i location of the base points in the interior. Thus, partial derivatives of these terms with respect to interior z's and r's will be equal to zero. If the derivatives had been taken with respect to the field points, these terms would not be equal to zero. It does make a difference, therefore, which set of points Equation (7) is taken with respect to.

In a manner analogous to that employed for the solution on the boundary, a $S_{\ker n_z}$ and $D_{\ker n_z}$, and a $S_{\ker n_r}$ and $D_{\ker n_r}$ can be defined such that:

$$\frac{\partial \phi_i}{\partial z} = \frac{1}{4\pi}\int_\Gamma \left[qS_{\ker n_z} - \phi D_{\ker n_z}\right] d\Gamma, \quad (34)$$

$$\frac{\partial \phi_i}{\partial r} = \frac{1}{4\pi}\int_\Gamma \left[qS_{\ker n_r} - \phi D_{\ker n_r}\right] d\Gamma, \quad (35)$$

where:

$$D_{\ker n_z} = \frac{-2(z-z_i)}{a^{3/2}}A - \frac{2}{\sqrt{a}}(B+C+H), \quad (36)$$

$$S_{\ker n_z} = \frac{16r^2 r_i(z-z_i)}{\sqrt{a^5}}F_1(p) + \frac{4r(z-z_i)K(p)}{\sqrt{a^3}}, \quad (37)$$

$$D_{\ker n_r} = \frac{2(r+r_i)}{\sqrt{a^3}}L - \frac{2}{\sqrt{a}}(M + NO - P), \quad (38)$$

$$S_{\ker n_r} = \frac{-8r\left[rr_i^2 - r^3 - r(z-z_i)^2\right]}{\sqrt{a^5}}F_1(p) - \frac{4(r+r_i)rK(p)}{\sqrt{a^3}}. \quad (39)$$

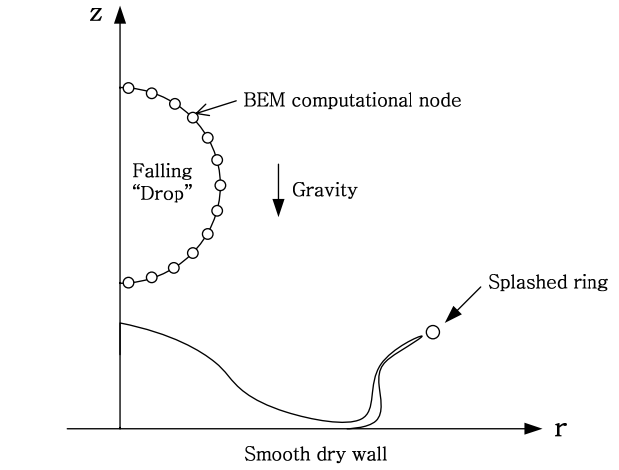

(a)

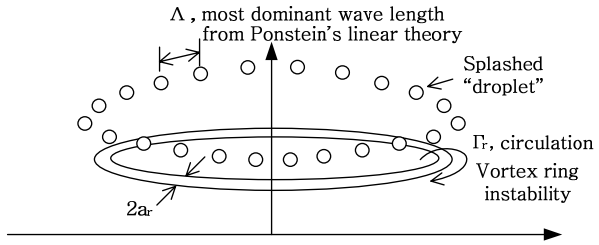

(b)

Figure 1. (a) Schematic of a falling "drop" toward a smooth dry plate within an axisymmetric computational domain. A corona arises upon impact and forms a splashed ring. (b) The BEM model assumes immediate vortex ring instabilty, which supposedly induces droplet formation, yielding splashed "droplets."

Equations (34) and (35) are then rewritten as a sum of integrals along each element. Because ϕ and q are assumed to vary linearly over the length of an element, the values of ϕ and q at any point on a given element bounded by nodes j and $j+1$ are:

$$\phi = \phi_j \frac{\Gamma_{j+1}-\Gamma}{\Gamma_{j+1}-\Gamma_j} + \phi_{j+1}\frac{\Gamma-\Gamma_j}{\Gamma_{j+1}-\Gamma_j}, \tag{40}$$

$$q = q_j \frac{\Gamma_{j+1}-\Gamma}{\Gamma_{j+1}-\Gamma_j} + q_{j+1}\frac{\Gamma-\Gamma_j}{\Gamma_{j+1}-\Gamma_j}, \tag{41}$$

where Γ is the distance of the point of interest from the starting end of the element. If terms $I_{1_{z,r}}$, $I_{2_{z,r}}$, $I_{3_{z,r}}$, and $I_{4_{z,r}}$ are defined so that:

$$I_{1_z} = \int_{\Gamma_j}^{\Gamma_{j+1}} \frac{\Gamma_{j+1}-\Gamma}{\Gamma_{j+1}-\Gamma_j} S_{\ker n_z}\,\mathrm{d}\Gamma, \tag{42}$$

$$I_{2_z} = \int_{\Gamma_j}^{\Gamma_{j+1}} \frac{\Gamma-\Gamma_j}{\Gamma_{j+1}-\Gamma_j} S_{\ker n_z}\,\mathrm{d}\Gamma, \tag{43}$$

$$I_{3_z} = \int_{\Gamma_j}^{\Gamma_{j+1}} \frac{\Gamma_{j+1}-\Gamma}{\Gamma_{j+1}-\Gamma_j} D_{\ker n_z}\,\mathrm{d}\Gamma, \tag{44}$$

$$I_{4_z} = \int_{\Gamma_j}^{\Gamma_{j+1}} \frac{\Gamma-\Gamma_j}{\Gamma_{j+1}-\Gamma_j} D_{\ker n_z}\,\mathrm{d}\Gamma, \tag{45}$$

and

$$I_{1_r} = \int_{\Gamma_j}^{\Gamma_{j+1}} \frac{\Gamma_{j+1}-\Gamma}{\Gamma_{j+1}-\Gamma_j} S_{\ker n_r}\,\mathrm{d}\Gamma, \tag{46}$$

$$I_{2_r} = \int_{\Gamma_j}^{\Gamma_{j+1}} \frac{\Gamma-\Gamma_j}{\Gamma_{j+1}-\Gamma_j} S_{\ker n_r}\,\mathrm{d}\Gamma, \tag{47}$$

$$I_{3_r} = \int_{\Gamma_j}^{\Gamma_{j+1}} \frac{\Gamma_{j+1}-\Gamma}{\Gamma_{j+1}-\Gamma_j} D_{\ker n_r}\,\mathrm{d}\Gamma, \tag{48}$$

$$I_{4_r} = \int_{\Gamma_j}^{\Gamma_{j+1}} \frac{\Gamma-\Gamma_j}{\Gamma_{j+1}-\Gamma_j} D_{\ker n_r}\,\mathrm{d}\Gamma, \tag{49}$$

and if we divide each of the integrals into two parts, Equations (36) and (37) are now:

$$\begin{aligned}\frac{\partial \phi_i}{\partial z} &= \int_\Gamma q_j \frac{\Gamma_{j+1}-\Gamma}{\Gamma_{j+1}-\Gamma_j} S_{\ker n_z}\,\mathrm{d}\Gamma + \int_\Gamma q_{j+1}\frac{\Gamma-\Gamma_j}{\Gamma_{j+1}-\Gamma_j} S_{\ker n_z}\,\mathrm{d}\Gamma \\ &- \int_\Gamma \phi_j \frac{\Gamma_{j+1}-\Gamma}{\Gamma_{j+1}-\Gamma_j} D_{\ker n_z}\,\mathrm{d}\Gamma - \int_\Gamma \phi_{j+1}\frac{\Gamma-\Gamma_j}{\Gamma_{j+1}-\Gamma_j} D_{\ker n_z}\,\mathrm{d}\Gamma \\ &= \sum_{j=1}^{n-1}\left[q_j I_{1(i,j)_z} + q_{j+1} I_{2(i,j)_z}\right] - \left[\phi_j I_{3(i,j)_z} + \phi_{j+1} I_{4(i,j)_z}\right],\end{aligned} \tag{50}$$

$$\begin{aligned}\frac{\partial \phi_i}{\partial r} &= \int_\Gamma q_j \frac{\Gamma_{j+1}-\Gamma}{\Gamma_{j+1}-\Gamma_j} S_{\ker n_r}\,\mathrm{d}\Gamma + \int_\Gamma q_{j+1}\frac{\Gamma-\Gamma_j}{\Gamma_{j+1}-\Gamma_j} S_{\ker n_r}\,\mathrm{d}\Gamma \\ &- \int_\Gamma \phi_j \frac{\Gamma_{j+1}-\Gamma}{\Gamma_{j+1}-\Gamma_j} D_{\ker n_r}\,\mathrm{d}\Gamma - \int_\Gamma \phi_{j+1}\frac{\Gamma-\Gamma_j}{\Gamma_{j+1}-\Gamma_j} D_{\ker n_r}\,\mathrm{d}\Gamma \\ &= \sum_{j=1}^{n-1}\left[q_j I_{1(i,j)_r} + q_{j+1} I_{2(i,j)_r}\right] - \left[\phi_j I_{3(i,j)_r} + \phi_{j+1} I_{4(i,j)_r}\right],\end{aligned} \tag{51}$$

The terms $I_{1_{z,r}} - I_{4_{z,r}}$ are calculated using Gaussian quadrature. To use Gaussian quadrature, the limits on the integrations are changed from (Γ_j, Γ_{j+1}) to $(-1,1)$. This is accomplished with the substitution:

$$\xi = \frac{\Gamma - \overline{\Gamma}}{\frac{\Delta\Gamma_j}{2}}, \tag{52}$$

where $\overline{\Gamma}$ is the average Γ over the interval. This gives:

$$\mathrm{d}\Gamma = \frac{\Delta\Gamma_j}{2}\mathrm{d}\xi. \tag{53}$$

Substituting this into Equations (44) through (51) reduces them to:

$$I_{1(i,j)_{z,r}} = \frac{\Delta\Gamma_j}{2}\int_{-1}^{1}\frac{1-\xi}{2} S_{\ker n_{z,r}}(\xi)\,\mathrm{d}\xi, \tag{54}$$

$$I_{2(i,j)_{z,r}} = \frac{\Delta\Gamma_j}{2}\int_{-1}^{1}\frac{1+\xi}{2} S_{\ker n_{z,r}}(\xi)\,\mathrm{d}\xi, \tag{55}$$

$$I_{3(i,j)_{z,r}} = \frac{\Delta\Gamma_j}{2}\int_{-1}^{1}\frac{1-\xi}{2} D_{\ker n_{z,r}}(\xi)\,\mathrm{d}\xi, \tag{56}$$

$$I_{4(i,j)_{z,r}} = \frac{\Delta\Gamma_j}{2}\int_{-1}^{1}\frac{1+\xi}{2} D_{\ker n_{z,r}}(\xi)\,\mathrm{d}\xi. \tag{57}$$

The values of $\partial\phi_i/\partial z$ and $\partial\phi_i/\partial r$ are determined after values of both ϕ and q have been calculated for every node on the boundary using the BEM solution to Laplace's equation. Because these values are already known, the D and S matrices are completely determined from the ϕ and q of nodes on the boundary and do not need to be integrated in time. Interior node calculations only have to be performed at times when data from the interior nodes are desired.

Vortex Ring Instability: Number of Splashed Droplets

It should be reminded that the current model is based on the axisymmetric formulation while the actual splashing phenomenon is a 3D event. To circumvent this inconsistency between reality and the axisymmetric model, we introduce a quasi-3D model and use Ponstein's linear theory [13], which predicts the most dominant wavelength along the rotating vortex ring shed from the periphery of the axisymmetric rising corona (see **Fig. 1**).

The most unstable wave number, k, is found implicitly from the maximum growth rate, ω. In dimension form, the relationship between k and ω is available by Ponstein's linear theory [13] for a rotating liquid column as follows:

$$\omega^2 = \left[\frac{\sigma}{\rho_l a_r^3}\left(1-k^2a_r^2\right)+\left(\frac{\Gamma}{2\pi a_r^2}\right)^2\right] ka_r \frac{I_1(ka_r)}{I_0(ka_r)}, \qquad (59)$$

where Γ is the circulation around the ring (or column) which can be estimated as $\Gamma = (2\pi a_r)V_\theta$ [14]. Here V_θ is the tangential velocity of the ring surface. $I_1(ka_r)$ and $I_0(ka_r)$ are modified Bessel functions of the first and second kind. For a non-rotating case (i.e. $\Gamma = 0$), Eq. (59) recovers Rayleigh's result [15] for liquid column instability, yielding the most dominant wavelength, $\lambda = 9a_r$. Here, circulation has a destabilizing effect as indicated by the positive sign on the Γ term. The faster the column rotates, the more unstable it becomes. The solution of Equation (59) yields the most unstable wave number (ka_r), determining the number of droplets (N) resulting from the breakup of this ring. The droplet diameters are calculated as functions of ring properties.

It is noteworthy that a nonlinear instability analysis will lead to multiple crests per wavelength [16-17] and subsequent smaller satellite droplets. In the present work, we ignore such nonlinear effects. Fortunately, this nonlinear effect is temporary; smaller waves from nonlinear effects disappear quickly upon capillary merging with other larger primary droplets during corona rising.

RESULTS AND DISCUSSION

A schematic of a falling drop onto a smooth substrate is shown in **Fig. 1**. The outer boundary for the gas domain, which is fixed in space, is large enough to encompass the liquid drop for the entire duration of the calculation. It is assumed that this outer boundary is placed far enough from the liquid domain that its influence on the flow field around a liquid drop is negligible. Therefore, a coarse grid can be used along this gas outer boundary. The impacting substrate is assumed to be smooth, dry plate. The boundary condition can be treated simply as a no flux condition through the wall, i.e. $q = 0$. Note here that the dissipative energy induced by the substrate's roughness is not considered in this model and, thus, the leftover post-impact energy of the liquid may be overestimated if the substrate's roughness is relevant.

Typical grid spacing, or the inter-node distance shown in **Fig. 1(a)**, used for the liquid drop's free surface with respect to the droplet radius is $ds/a = 0.02$; thus, approximately 157 nodes were implemented along the free surface at the start of the computation. Upon the impact, the morphology of the drop changes resulting in longer free surface lengths and requiring more computational nodes.

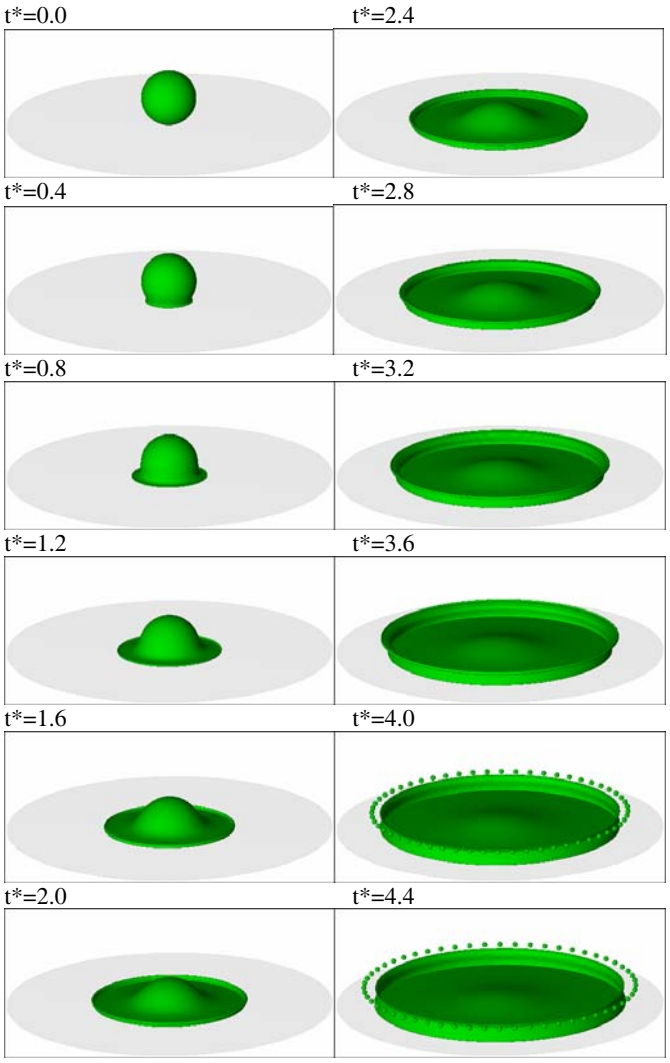

(a)

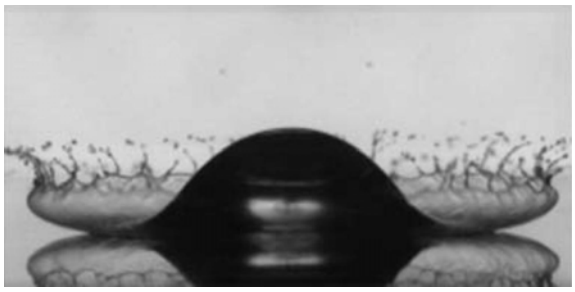

(b)

Figure 2. (a) Formation of the rising corona and the subsequent splashed droplets, whose number is predicted by the vortex ring instability of Ponstein's linear theory. The impact condition at which this simulation was carried out is based on the Xu et al. [9] experiment: imapct speed, U = 3.74 m/s; drop radius is a = 1.7 mm; Weber number, We = 838; Bond number, Bo = 0.998. (b) A snapshot of the splashing from Xu et al.'s experiment.

The drop center was initially located $4a$ above the substrate's wall with an air pressure of 1 atm. Because the drop's dimensionless radius is unity (e.g., the reference length is the drop's radius), the drop's bottom is situated at $z = 3$. Thus, there are $\Delta t^* = \Delta tU/a = 3$ dimensionless time units before impact. At the instant of release, the drop has initial impact

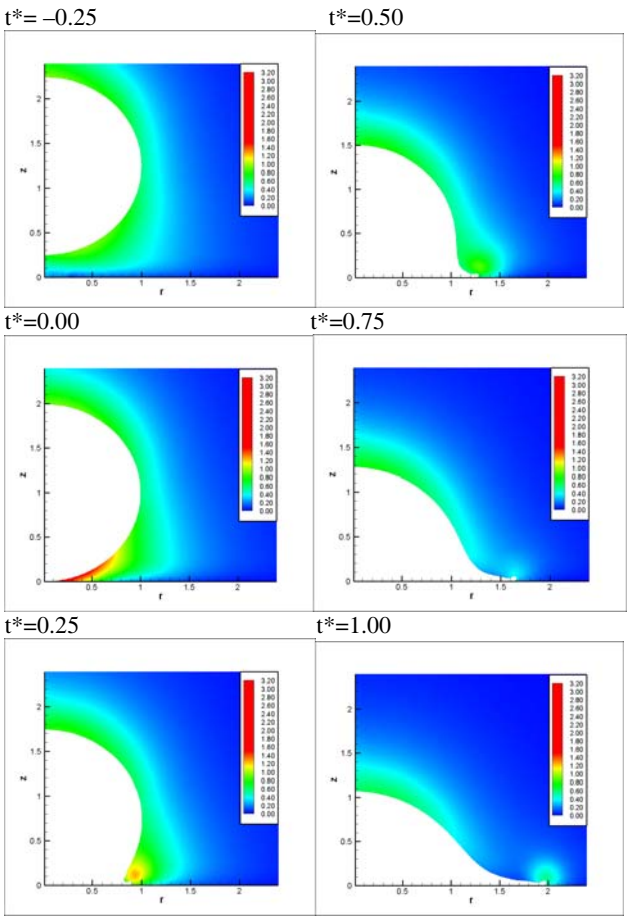

Figure 3. The time series variation of the gas flux contour outside the drop at *We* = 200. The induced gas flux reaches up to 3 times of the drop's falling or impact speed (which is unity at the reference speed); see the snapshot at the dimensionless time, $t^* = (U/a)t = 0$.

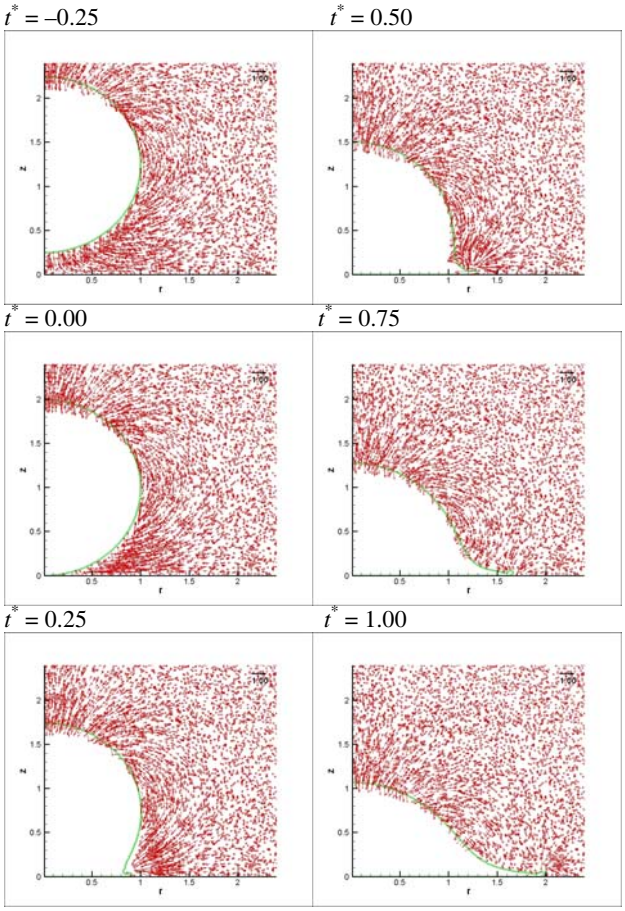

Figure 4. The time series variation of the gas flux vector in conjuction with Figure 3.

speed, U_i, and the velocity gained due to conversion of potential energy with $h = 4a$ is ignored because the final impact speed is approximated by $U_f = \sqrt{U_i^2 + 2gh}$, where the magnitude of the $2gh$ term comprises only 0.1% (or less) of the total speed, U_f, for Xu et al.'s case; thus, $U_f \sim U_i$.

Several numerical runs confirmed that the, $h = 4a$ starting condition was sufficiently far from the wall to introduce minimal gas pressure buildup. Previous grid-convergence studies [8] confirmed a good collapse of data for the various grid sizes and an indicate the solution's independence of the grid spacing. It should be noted that at high Weber numbers, using a sufficient number of computational nodes near the impact region is critically important to capture the detailed physics of splashing.

Figure 2 shows the time series snapshots of the splashing event for Xu et al's case [9], starting from $t^* = 0.0$. The impact instance is set as the $t^* = 0.0$ while the simulation was initiated at $t^* = -3.0$. It took about $t^* = 4.0$ (equivalent to the real time, $t = t^* a/U = (4 \times 0.0017 \text{ m}/3.74 \text{ m/s} = 1.82 \text{ ms})$ for the rising corona to elongate and finally snap off. Upon snap off, Ponstein's linear theory was applied and it predicts 56 splashed droplets while the corresponding experimental images indicate approximately 52 ± 2 splashed droplets at the rim of the crown; see **Figure 2(b)**. The comparison between the model's prediction and the experiment is fairly good.

Figures 3 and **4** show interior fluxes (both speed and velocities). For high computational resolution, enough random points (5,000) were seeded into the region of interest. As expected, at the instance of impact (i.e., $t^* = 0.00$), the air is accelerated with maximum speed about $3.3U$ right beneath the drop's bottom surface. This high air speed, suddenly generated at the drop surface, yields sufficient vorticity to provide the disturbance that eventually leads to splashing.

The BEM Green's function kernels derived for the interior random points from Equation (34) and (35) are also applicable for computing the liquid fluxes. Providing the boundary values of ϕ_l and q_l as inputs for the Equations (34) and (35) yields the liquid fluxes at various instances as shown in **Figure 5**. The "green" color contour indicates the dimensionless impact speed 1.0; see the drop falling snapshot at $t^* = -0.25$. Upon impact, the contacting liquid is, of course, stagnant and its flux approaches zero while that of the spreading edge accelerates in the direction of the accelerated air shown in **Figures 3 and 4**. Basically, momentum was transferred from the falling drop to the air. Then, the accelerated air entrains the liquid edge and the corona follows. Eventually, splashing occurs.

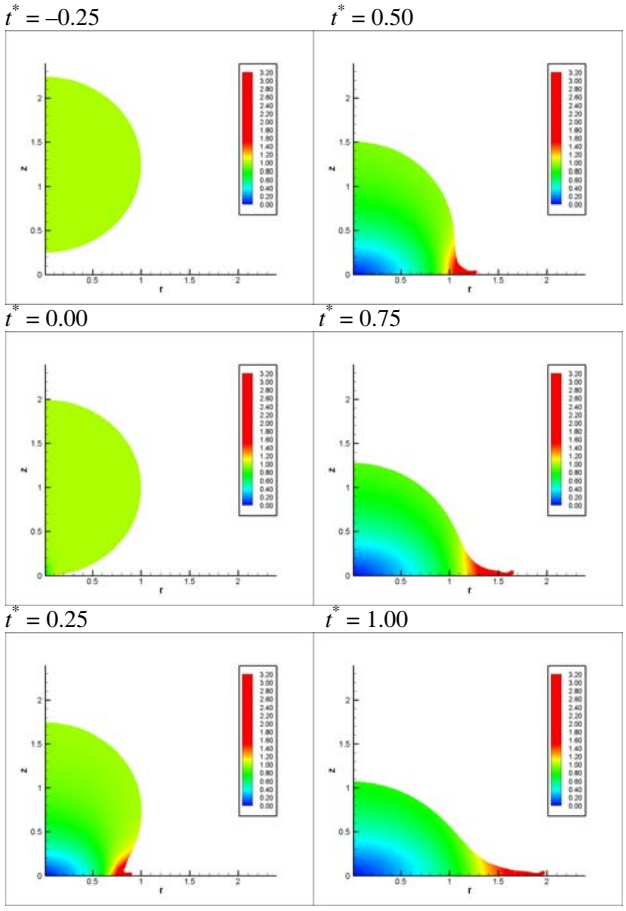

Figure 5. The time series variation of the liquid flux contour inside the drop at *We*=200.

CONCLUSION

The BEM was applied to model the compressed air effect on drop splashing when a drop impacts onto a smooth, dry plate. We computed the interior gas fluxes by taking derivatives of the velocity potential, which comprises the integral of the derivatives of the Green's function. Our preliminary computations showed that the air velocity reached in excess of 3 times the drop's impact speed. This escaping air may contain sufficient momentum and shear force to rupture the drop surface. This shear-driven instability may eventually lead to splashing (the *milk-drop crown* effect). Our BEM splash model is unique in that: (*i*) the field properties (such as *fluxes*) of both liquid and gas phases were assessed, (*ii*) air compression due to a falling drop was taken into consideration, (*iii*) the number of splashed droplets was predicted using Pontein's linear theory of vortex-ring instability. At this point in the model development, further model verification and parametric studies are needed to confirm the validity and extended capabilities of the model.

ACKNOWLEDGMENT

The authors acknowledge that this work was supported by the Korea Research Foundation Grant funded by the Korean Government (MOEHRD), KRF-2007-331-D00061.

REFERENCES

[1] A.M. Worthington, On the Forms Assumed by Drops of Liquids Falling Vertically on a Horizontal Plate., *Proc. R. Soc. London A.*, vol. 25, pp. 261, 1876

[2] A.M. Worthington, On the Forms Assumed by Drops of Liquids Falling Vertically on a Horizontal Plate., *Proc. R. Soc. London A.*, vol. 25, pp. 498, 1877

[3] S.D. Aziz and S. Chandra, Impact, Recoil and Splashing of Molten Metal Droplets, *International Journal of Heat and Mass Transfer*, vol.43, pp. 2841–2857, 2000

[4] A.L. Yarin and D.A. Weiss, Impact of Drops on Solid Surfaces: Self-Similar Capillary Waves, and Splashing as a New Type of Kinematic Discontinuity, *Journal of Fluid Mechanics*, vol. 283, pp. 141–173, 1995

[5] D.A. Weiss and A.L. Yarin, Single Drop Impact onto Liquid Films: Neck Distortion, Jetting, Tiny Bubble Entrainment, and Crown Formation, *Journal of Fluid Mechanics*, vol. 385, pp. 229–254, 1999

[6] M.R. Davidson, Boundary Integral Prediction of the Spreading of an Inviscid Drop Impacting on a Solid Surface, *Chemical Engineering Science*, vol. 55, pp. 1159–1170, 2000

[7] M.R. Davidson, Spreading of an Inviscid Drop Impacting on a Liquid Film, *Chemical Engineering Science*, vol. 57, pp. 3639–3647, 2002

[8] H. Park, S.S. Yoon, R.A. Jepsen, S.D. Heister, H.Y. Kim, Droplet Bounce Simulations and Air Pressure Effects on the Deformation of Pre-Impact Droplets, using a Boundary Element Method, *Engineering Analysis with Boundary Elements*, vol. 32, pp. 21–31, 2008

[9] L. Xu, W.W. Zhang, S.R. Nagel, Drop Splashing on a Dry Smooth Surface, *Physical Review Letters*, vol. 94, 184505, 2005

[10] L. Xu, Liquid Drop Splashing on Smooth, Rough, and Textured Surfaces, *Physical Review E*, vol. 75, 056316, 2007

[11] S.D. Heister, Boundary Element Methods for Two-Fluid Free Surface Flows, *Engineering Analysis with Boundary Element*, vol. 19, pp. 309–317, 1997

[12] C.A. Spangler, J.H. Hilbing, S.D. Heister, Nonlinear Modeling of Jet Atomization in the Wind-Induced Regime, *Physics of Fluids*, vol. 7, pp.964–971, 1995

[13] J. Ponstein, Instability of Rotating Cylindrical Jets, *Appl. Sci. Res.*, vol. 8, no. 6, pp. 425–456, 1959

[14] P.G. Saffman, The Number of Waves on Unstable Vortex Rings, *J. Fluid Mech.*, vol. 84, pp. 625–639, 1978

[15] W.S. Rayleigh, On the Instability of Jets, *Proc. Lond. Math. Soc.*, vol. 10, no. 4, 1878

[16] M. C. Yuen, Non-linear capillary instability of a liquid jet, *J. Fluid Mech.* vol. 40, pp. 495, 1970

[17] P. Lafrance, Nonlinear breakup of a liquid jet, *Phys. Fluids*, vol. 17, pp. 1913, 1974